



Contents lists available at ScienceDirect

International Journal of Solids and Structures

journal homepage: www.elsevier.com/locate/ijsolstr

Harnessing local flow in buckling pores for low-frequency attenuation

Patrick Kurzeja^{a,*}, Beatriz Quintal^b

^a Institute of Mechanics, TU Dortmund University, 44227 Dortmund, Germany

^b Institute of Earth Sciences, University of Lausanne, 1015 Lausanne, Switzerland

ARTICLE INFO

Keywords:

Instability

Local flow

Squirt flow

Porous media

Attenuation

Fluid–structure interaction

ABSTRACT

While attenuation at low frequencies remains highly desirable for industrial applications such as multistory buildings or spacecraft propellant tanks, fluid-filled rocks can achieve this goal naturally by so-called local flow in their heterogeneous pore structure. The present work aims at combining this natural phenomenon with controlled instabilities in light-weight structures. Buckling of their pores is harnessed to break local geometric symmetry and maximize the local-flow effect. A prototype structure with elliptical pores is analyzed numerically. It does not show local flow or attenuation for the starting geometry, but reversibly switches into an attenuating structure by imposing a critical buckling strain. The simulations reach inverse quality factors larger than 0.3 around 5 Hz for material properties of air-filled silicone rubber. A key to high attenuation is a tradeoff between the unstable structure and the pore fluid. If the solid is too soft, the fluid-filled pores are not compressed and buckling is not triggered. If the solid is too stiff, most energy is stored elastically and not dissipated by fluid flow. The proposed, fluid-filled structure allows for a scalable, light-weight material exhibiting significant low-frequency attenuation.

1. Introduction

Materials and structures capable of effectively dissipating mechanical energy play a crucial role in a wide range of systems, including buildings, automobiles, aircrafts, and micro-scale electric devices. Although several strategies have been proposed to achieve the desired values of attenuation, dissipation at low frequencies still poses major challenges. Internal resonances in structures or saturated porous media provide a significant amount of attenuation for special frequency bands, but are typically restricted to higher frequencies or larger spatial dimensions, e.g., air curtains (Würsig et al., 2000), foams (Chevillotte et al., 2013) or oscillating fluid clusters (Kurzeja and Steeb, 2014a,b). Also modern architectures such as auxetic metamaterials (Ungureanu et al., 2015), phononic plates (Hedayatrasa and Kersemans, 2022) and piezoelectric metamaterials (Jian et al., 2022) successfully aim at broad and tunable bandgaps that yet do not reach seismic frequencies with small sizes. Flow in open porous media can reach attenuation at low frequencies but is not scalable, since it requires a connection to the surrounding air or an additional reservoir for fluid exchange (Pierre et al., 2014). Polymers generally combine favorable production conditions with significant attenuation, which is however dependent on a restricted temperature range (Gibson and Ashby, 1999; Pritz, 1994; Lu et al., 1999; Kazakevičiūtė-Makovska et al., 2014). This is improved in composites with visco-elastic fillers (Chung, 2001, 2003) and asphalt (Schüler et al., 2013; Dickinson and Witt, 1974), but again by

paying the price of very large mass or size for significant low-frequency damping. Finally, phase-transforming composites materials can rely on damage that is not acceptable in many applications (Junker and Kochmann, 2017).

Interestingly, a significant low-frequency attenuation mechanism has been observed in fluid-filled rocks (Pimienta et al., 2015a,b; Subramaniyan et al., 2015; Borgomano et al., 2019; Chapman et al., 2019). Local flow is triggered by the uneven deformation of fluid-filled regions with different compliances, see Fig. 1(a) for illustration. A review of the underlying fluid-flow related mechanisms can be found in (Müller et al., 2010) and (Gurevich and Carcione, 2022). For example, local flow at the pore scale is often referred to as squirt flow and is caused by fluid displacement between interconnected compliant and stiff pores (Mavko and Nur, 1975; O'Connell and Budiansky, 1977; Jones, 1986; Dvorkin and Nur, 1993; Dvorkin et al., 1994; Gurevich et al., 2010; Adelinet et al., 2011; Shapiro, 2013; Borgomano et al., 2019; Alkhimenkov and Quintal, 2022a,b). For example, in the heterogeneous pore structure of a Berea sandstone (Ohio, USA) (Fig. 1(b)), compliant pores are represented by the grain contacts and the more isometric pores are the stiff ones. In fractured media, local flow occurs between the cracks and the porous host matrix or between differently oriented interconnected cracks (Brajanovski et al., 2005; Rubino et al., 2013; Vinci et al., 2014; Quintal et al., 2016). Variations in saturation constitute another origin

* Corresponding author.

E-mail address: Patrick.kurzeja@tu-dortmund.de (P. Kurzeja).

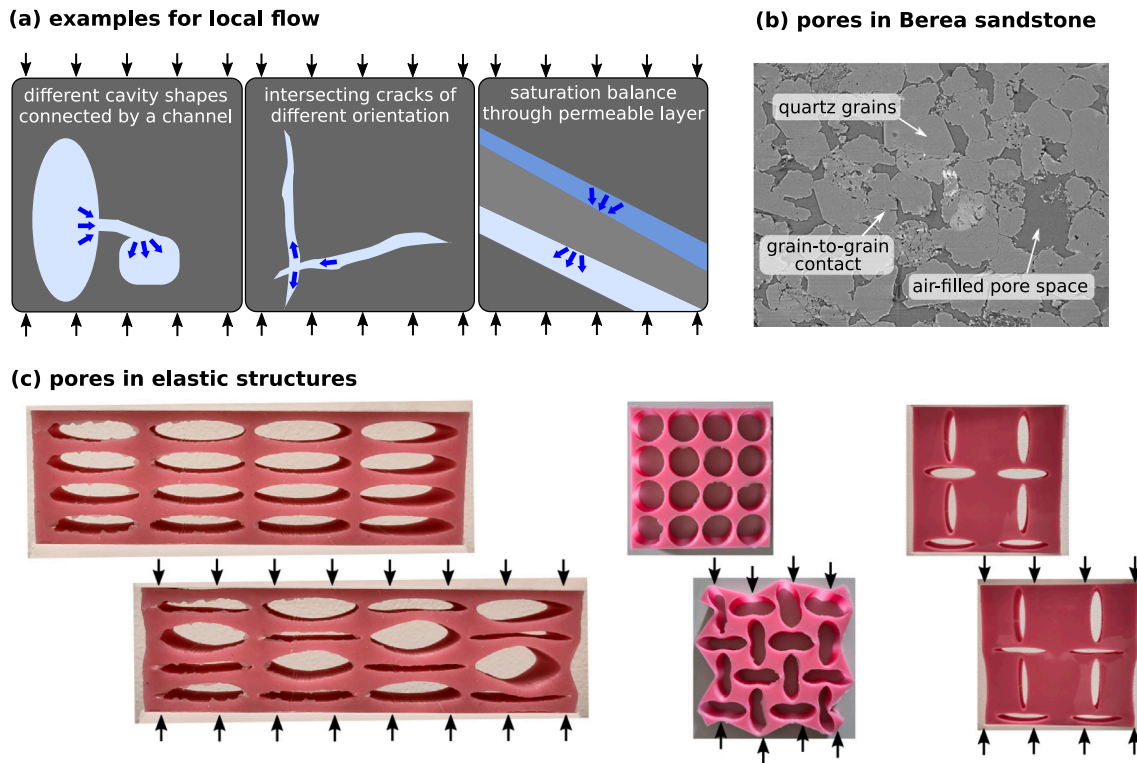


Fig. 1. (a) Examples of systems prone to local flow. Compression induces heterogeneous volumetric changes of the fluid-filled regions and thus causes dissipative fluid flow between them. (b) Pore structure of a dry Berea sandstone (Ohio, USA) from Madonna et al. (2013). Its porosity is approximately 20% and the width of the section is 650 μm . (c) Pores in highly elastic structures cast from duplicating silicone Zhermack Elite Double 8.

for local-flow attenuation (White et al., 1975; Dutta and Odé, 1979a,b; Tisato and Quintal, 2013; Quintal et al., 2011). Only few attempts have yet been made to utilize local-flow in artificial materials. Its general potential has been shown for large strains, e.g. Cohen et al. (2017), but a detailed understanding on the pore level is yet missing.

It has been recently shown that mechanical instabilities can result in dramatic pattern transformations. The diverse applications include load-induced adaptations through shape morphing (Reksowardojo et al., 2022), inverse metamaterial design (Dos Reis and Karathanasopoulos, 2022) or band gaps in elastomeric structures with periodic distributions of holes (Bertoldi and Boyce, 2008a,b; Bertoldi et al., 2008; Overvelde et al., 2012), see Fig. 1(c) for illustrating examples. In contrast to rocks, elastomeric structures provide drastic and yet reversible shape changes at much lower weight. Although mechanical instabilities in geological formations are also known in the form of folding and necking (Ramsay and Huber, 1987; Hudleston and Treagus, 2010), buckling with fold amplification (Schmalholz and Podladchikov, 1999) or high-pore-pressure faulting (Miller, 2002; Geli et al., 2014), attenuation modulation by non-linear deformation in architected materials just opened as an opportunity (Cohen et al., 2017). Also other research areas recently allowed for significant insights into the response of fluid-filled structures such as batteries (Carlstedt et al., 2022) or bilayer porous metamaterials (Esposito et al., 2022). A detailed understanding of the fluid–structure interaction in instable structures however remains to be fully explored. More specifically, an interesting question to ask is whether local flow mechanisms can also be activated in highly deformable porous structures and what is their effect.

The present work aims at numerically exploring the potential of buckling pores with the highest possible attenuation. As most studies employ local flow as a naturally predetermined process in their systems, the present work turns the view to the following novel key questions:

- what conditions make structures susceptible to local flow?
- how can severely buckling pores amplify local flow?

- what geometric and material parameter settings eventually yield the highest attenuation at low frequencies?

In what follows, we first introduce the system of interest and the methodology in terms of material modeling and numerical implementation in Section 2. Most promising dry structures are then identified with respect to their ability to locally displace fluid in Section 3. Choosing a prototype structure with elliptical pores, the peak attenuation and its associated frequency are finally studied for various buckled states, stiffness ratios and geometric modifications in Section 4. In Section 5, we present our conclusions along with a comparison with other attenuation mechanisms and implications for fluid-filled artificial materials with instabilities.

2. Methodology

2.1. The idealized unit cell

The system of interest is idealized in Fig. 2 and can be divided into the elastic host matrix, the pore fluid and connections between the pores. As the present study aims at harnessing the local-flow principle, the solid material focuses on elastic structures that can be 3D-printed or cast such as flexible filament or silicone rubber. The elastic solid shall hence be described by a slightly compressible neo-Hookean model (Ogden, 1997) with strain energy density

$$W = \frac{\mu_s}{2}(\bar{I}_1 - 3) + \frac{K_s}{2}(J - 1)^2, \quad (1)$$

where \mathbf{F} is the deformation gradient, $J = \det(\mathbf{F})$, $\bar{I}_1 = J^{-2/3} \text{tr}(\mathbf{F}^T \mathbf{F})$ and μ_s and K_s are the solid’s initial shear and bulk modulus, respectively.

The pores are assumed to be filled with a barotropic fluid, so that

$$\frac{\partial \rho_f}{\partial p} = \frac{\rho_{f,0}}{K_f}, \quad (2)$$

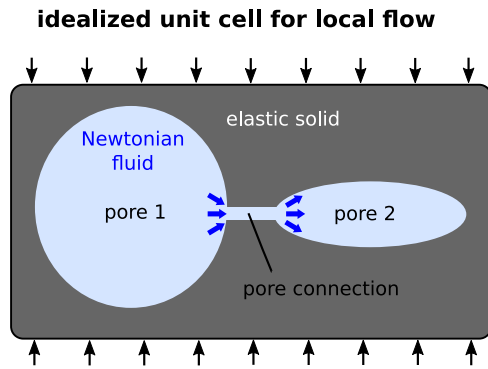


Fig. 2. Sketch of a reduced and idealized local-flow unit cell.

where K_f is the fluid bulk modulus, p is the pressure of the fluid inside the pore and $\rho_{f,0}$ and ρ_f are the fluid density in the initial (i.e. at $p = 0$) and deformed configuration.

The connections are assumed to allow laminar flow for fluid exchange, e.g., in the form of a cylindrical puncture between the two pores. Accordingly, we assume that pairs of neighboring pores can exchange fluid and that the rate of mass exchange follows Poiseuille's law

$$\frac{dm}{dt} = -\rho_f \gamma \Delta p, \quad (3)$$

$$\gamma = \frac{\kappa A}{l \eta}, \quad (4)$$

where Δp is the fluid pressure difference between the two connected pores, η is the dynamic fluid viscosity and κ , A and l denote the permeability, cross sectional area and length of the connections. The latter four can be combined to the conductivity parameter γ . Note that these connections are assumed not to interfere with the deformation, e.g., in the form of small pores or channels that do not significantly alter the solid deformation.

Inertia terms are artificially neglected in this study in line with previous studies of local flow, i.e., wave propagation and resonance effects are not accounted for. They exceed the scope of the present work towards higher frequencies and would later require much smaller time steps and computational costs. The relevant frequencies of maximum attenuation are around 5 Hz with wave lengths in the order of 10 m. Non-linearities are especially considered for geometric modulation of the buckling structure. Non-linear fluid behavior is nevertheless assumed to be negligible, because of the small dynamic perturbations used for subsequent attenuation measurements. Small Reynolds and Womersley numbers are hence assumed in combination with the low-frequency regime. This study focuses on two-dimensional simulations, e.g., assuming extruded structures with connections in the form of holes or channels distributed along the extrusion depth.

The initial material parameters throughout this paper are based on a soft silicone rubber-air system with a single connecting pore per unit meter depth of 0.6 mm diameter. The specific values read $\mu_s = 3.45$ MPa, $K_s = 33.33$ MPa, $E_s = 10.00$ MPa, $K_f = 0.1$ MPa, $\eta = 17.1 \times 10^{-6}$ Pa s and $\gamma = (\kappa A)/(l \eta) = 9.75 \times 10^{-8} \text{ m}^3 \text{ Pa}^{-1} \text{ s}^{-1}$, unless scaled for parameter tests.

2.2. An analytical approximation for a local-flow cell

In line with local flow in rocks, the so-called inverse quality factor Q^{-1} will be used as a measure of attenuation and serves as a leading focus of the present study. More specifically, two particular values will be studied, the maximum value of the inverse quality factor Q_{max}^{-1} and its associated frequency f_{max} . Q^{-1} depends on frequency f and various definitions can be found in literature (O'Connell and Budiansky, 1977; Graesser and Wong, 1991; Ursin and Toverud, 2002; Mavko

et al., 2009). Most definitions resemble the ratio of energy dissipated to total energy stored at small amplitudes. As such Q^{-1} is a relative and dimensionless measure of attenuation. It shall be defined in the present context as the absolute ratio of loss modulus $\Im(M)$ and storage modulus $\Re(M)$, reading

$$Q^{-1}(f) = \left| \frac{\Im(M)}{\Re(M)}(f) \right|. \quad (5)$$

In order to guide the initial design of pore geometries exhibiting local flow, we may first approximate the inverse quality factor for a local-flow unit cell, cf. Fig. 2. The following notable assumptions shall be summarized: a virtually incompressible hyperelastic solid, structural stiffness much lower than the solid bulk stiffness, a barotropic fluid, laminar flow through the connection but negligible within the pores and a linearized perturbation for the dynamic analysis fitted by a Standard-Linear-Solid rheology. These assumptions are clearly simplifying the situation in a rock matrix. The analytical approximation will nevertheless help to guide the design process and to understand the limitations and opportunities of the resulting, regular prototype structure.

Combining the relationships from the above Section 2.1 eventually yields the governing equation between a linear strain perturbation of the overall unit cell $\Delta \epsilon$ and the pressure response in the first pore Δp_1 (see Appendix A for details)

$$\Delta \dot{p}_1 + \Delta p_1 \left[2 \frac{K_f}{V_0} \gamma \right] + \Delta \dot{\epsilon} \left[\frac{\Delta V_1}{\Delta \epsilon} \frac{K_f}{V_0} \right] + \Delta \epsilon \left[\gamma \left(\frac{\Delta V_1 + \Delta V_2}{\Delta \epsilon} \right) \left(\frac{K_f}{V_0} \right)^2 \right]. \quad (6)$$

V_0 is the pores' initial volume and the ratio $\Delta V_j/\Delta \epsilon$ describes the susceptibility of volume changes in pores $j \in \{1, 2\}$. Knowing the pressure relaxation response allows to derive the associated moduli and to add them to the elastic modulus of the solid frame M_{extra} (see again Appendix A for details). As an intermediate result, the entire local-flow cell exhibits the rheological behavior of a Standard Linear Solid (SLS)-model or Zener model (de Haan and Sluimer, 2001), which was also confirmed by the simulations (cf. Appendix B). The corresponding static modulus and dynamic modulus read

$$M_{\text{stat}} = M_{\text{extra}} + \frac{K_f}{2 V_0^2 \epsilon^2} (\Delta V_1 + \Delta V_2)^2, \quad M_{\text{dyn}} = \frac{K_f}{2 V_0^2 \epsilon^2} (\Delta V_1 - \Delta V_2)^2. \quad (7)$$

The moduli and the SLS-rheology of the local-flow cell allow to finally approximate its inverse quality factor by

$$Q^{-1}(f) = \frac{(f/f_c) \Delta V^2}{c + (f/f_c)^2 (c + \Delta V^2)}. \quad (8)$$

This format explicitly depends on three key properties. Firstly, the volume exchanged between both pores

$$\Delta V = \Delta V_1 - \Delta V_2, \quad (9)$$

secondly, the analytical characteristic frequency

$$f_c = \frac{1}{\pi} \frac{K_f}{V_0} \gamma \quad (10)$$

and thirdly

$$c = 2 V_0^2 \Delta \epsilon^2 \frac{M_{\text{extra}}}{K_f} + (\Delta V_1 + \Delta V_2)^2 = M_{\text{stat}} \frac{K_f}{2 V_0 \Delta \epsilon^2}. \quad (11)$$

Consistent with the linear approach and with well-accepted approximations for local-flow in literature, the analytical characteristic frequency f_c is not influenced by the amount of volume changed. It is proportional to the ratio of elasticity to viscosity and the geometric properties typically scale with an exponent between 2 and 4 (O'Connell and Budiansky, 1977; Dvorkin and Nur, 1993; Ciz et al., 2006; Gurevich et al., 2010; Alkhimenkov and Quintal, 2022a,b). The presented analytical approximation will thus serve as a reference for interpretation of the subsequent analysis. The term c accounts for the

remaining static resistance to cell deformation $\Delta\epsilon$, normalized by the fluid's compressibility-volume ratio.

An important conclusion can be made at this point by specifying goals for harnessing local flow for attenuation at low frequencies — even though the sensitivities to deformation of the pores ($\Delta V_j/\Delta\epsilon$) and the solid structure (M_{extra}) have not yet been specified. In general, low-frequency attenuation is potentially pronounced for soft structures (small c and small K_f/V_0) with low conductivity (small γ) displacing much fluid (large ΔV). Architected materials with mechanical instabilities offer a promising framework for local flow because of their dramatic shape changes and low stiffness. The first key focus of this study will be the maximization of ΔV between dry pores before the most promising, fluid-filled geometry will be examined in detail.

2.3. Test setup and loading conditions

2.3.1. Dry pore structures

Three classes of pore structures will be first examined with respect to local pore volume changes ΔV under compression in Section 3. This property is emphasized first as it provides high potential for improving the local-flow effect in artificial structures by design.

2.3.2. Prototype unit cell

A structure with elliptical pores will be chosen as a prototype for the fluid-filled investigations, see Fig. 3 for illustration. Both infinitely periodic structures and finite-sized structures are considered. Starting from a relaxed system, two vertical loading conditions are applied consecutively for a finite pre-compression $\epsilon_{\text{pre}} = 0\%, -1\%, -2\%, \dots, -10\%$:

1. non-linear, quasi-static step: to achieve pre-compression at ϵ_{pre}
2. linear, dynamic perturbation: to evaluate Q^{-1}

The pre-compression is increased stepwise to test when and how buckling instabilities turn the pore architecture into a mode allowing for local flow. The small dynamic perturbation is used to determine the attenuation at these pre-compressed states.

For the periodic unit cell, the macroscopic deformation gradient, $\bar{\mathbf{F}} = \mathbf{e}_1 \otimes \mathbf{e}_1 + (1 + \epsilon) \mathbf{e}_2 \otimes \mathbf{e}_2 + \mathbf{e}_3 \otimes \mathbf{e}_3$, is imposed on the cell boundaries by periodic boundary conditions (Danielsson et al., 2002; Bertoldi and Boyce, 2008b)

$$u_\alpha^{A_i} - u_\alpha^{B_i} = (\bar{F}_{\alpha\beta} - \delta_{\alpha\beta})(X_\beta^{A_i} - X_\beta^{B_i}), \quad i = 1, 2, \dots, N \quad (12)$$

where $\delta_{\alpha\beta}$ is the Kronecker delta, $u_\alpha^{A_i}$ and $u_\alpha^{B_i}$ ($\alpha = 1, 2$) are displacements of points periodically located on the boundary of the unit cell. Moreover, N denotes the number of pairs of nodes periodically located on the boundary of the unit cell. Also note that another (horizontal) compression direction would induce a different buckling pattern with equal volume changes in all pores, which is not useful to trigger local flow.

2.4. Numerical implementation

The nonlinear finite-element code Abaqus Standard 6.14-2 is used to pre-compress the structures as well as for dynamic perturbations in order to investigate the ability of the predeformed systems to dissipate energy in the small-strain regime. For all the analyses, 2D finite element models are constructed using four-node plane strain elements (Abaqus element type CPE4R) and the accuracy of the mesh is ascertained through a mesh refinement study. The dynamic response is simulated in the time domain (Quintal et al., 2011, 2016) conducting dynamic implicit simulations (*DYNAMIC module in Abaqus). Fluid flow is implemented by additional interaction conditions inside and between the pores. More specifically, the state inside the pores is determined from the linearized pressure-volume relationship in Eq. (2). The mass flow between two pores is calculated from their pressure difference

with the proportionality factor as stated in Eq. (3) assuming laminar fluid exchange.

To focus on the effect of local flow, we make use of the following assumptions to reduce the computational effort (Quintal et al., 2011, 2016; Vinci et al., 2014; Jänicke and Steeb, 2015). Firstly, a uniform pressure distribution is assumed in each pore. Pressure-driven viscous flow is much more dominant in the connections between the pores and not within the larger pores. Secondly, the flow is assumed to be laminar due to the small frequencies and cross-sectional area yielding small Reynolds and Womersley numbers. Thirdly, inertia terms are artificially neglected by lowering the fluid and solid densities to the order of $\rho_{f,0} = 1 \text{ kg/m}^3$ and $\rho_{s,0} = 0.005 \text{ kg/m}^3$, i.e., wave propagation and resonance effects are not resolved as they exceed the scope of the present work. Note that these assumptions do not overestimate attenuation.

The numerical implementation of all loading steps adds extra relaxation periods to reach equilibrium before the other step continues. The numerical time stepping scales inversely to the approximated characteristic frequency f_c in Eq. (10) to accurately resolve the physical phenomenon. The numerical steps or durations, considering a finite pre-compression $\epsilon_{\text{pre}} = 0\%, -1\%, -2\%, \dots, -10\%$, are:

1. Quasistatic pre-compression step
 - apply ϵ_{pre} by linear ramp (duration: $30 f_c^{-1}$)
 - let the new configuration relax (duration: $20 f_c^{-1}$)
2. Dynamic perturbation step
 - apply perturbation $\delta\epsilon = -0.001\%$ by linear ramp (duration: $\approx 0.035 f_c^{-1}$)
 - hold perturbation to relax (duration: $\approx 3.5 f_c^{-1}$)

Note that the characteristic frequency adapts automatically to the material and geometric variations of the parameter studies. The time scaling of the dynamic steps, however, has been fine-tuned around the approximative values given above, because f_c is an idealized approximation that does not account for boundary effects in finite-size structures, for instance.

The inverse quality factor is finally calculated from the stress response of the dynamic strain perturbation by a fast fourier transformation (FFT). This result is double checked with a rheological fit (cf. Appendix B). Furthermore, the numerical settings were tested carefully in a sensitivity study including mesh size, perturbation amplitude and relaxation time (cf. Appendix C).

3. Pore structures with maximum potential for fluid volume exchange

While rock formations naturally show the ability for local fluid flow, we will instead choose pores that show more significant morphology changes when buckling to explore new potentials in pore architectures. The goal is to maximize the potential fluid exchange between pores measured by volume ΔV . Focusing on the role of the structure first, we will compute the volume changes in dry pores from finite element simulations as described in Section 2.4.

Three types of periodic cells with different, characteristic pores are investigated. Demonstrators have been cast for previous illustration in Fig. 1(c) and are color-coded in Fig. 4 from bottom to top: perpendicular ellipses (blue), circular pores (red) and parallel ellipses (black). The first one is an idealized representation for basic, natural local flow, e.g., cracks or elongated cavities that may appear with different orientations (Müller et al., 2010; Collet and Gurevich, 2016; Adelinet et al., 2011; Gurevich and Carcione, 2022) and has also been used in artificial design (Cohen et al., 2017) and pressure polarization analysis (Shafiro and Kachanov, 1997). The second type is a regular array of circular holes, which is a well-known representation of buckling structures in general. The third type is a regular array of elliptical pores, which is a

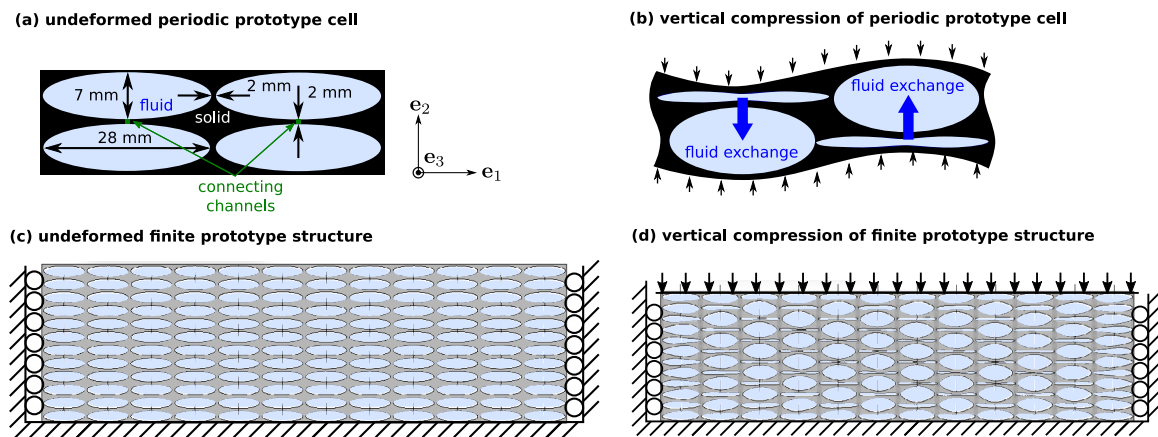


Fig. 3. (a) Sketch of the undeformed prototype cell, (b) vertically compressed periodic prototype cell, (c) undeformed finite prototype structure, and (d) vertically compressed finite prototype structure. Each consecutive pair of vertically adjacent pores is connected by a channel, which is indicated by thin black lines in the finite prototype structure.

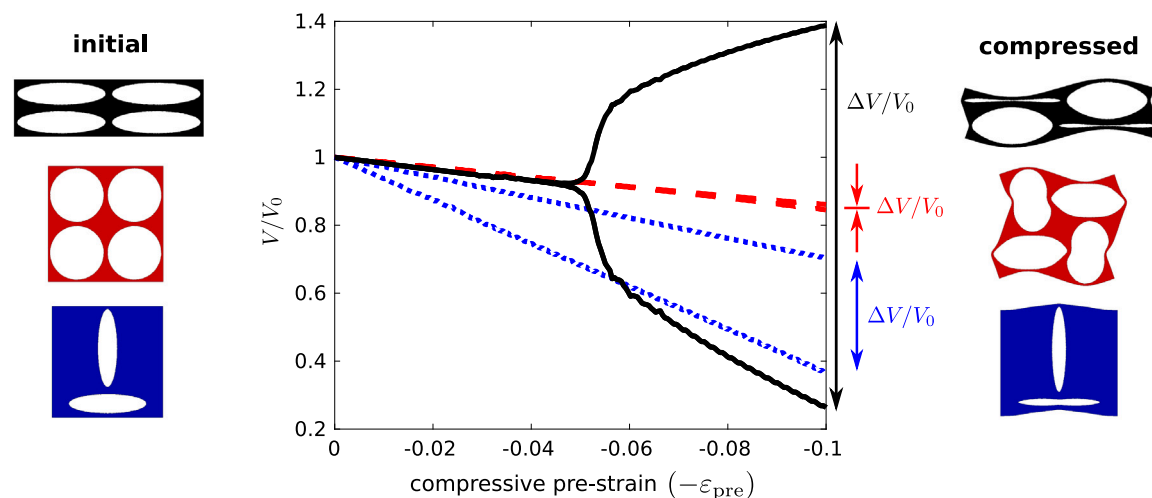


Fig. 4. Normalized volumes of adjacent pores in three periodic, dry structures under finite vertical pre-compression: parallel elliptical pores (black), circular pores (red) and perpendicular elliptical pores (blue). The goal for maximized local fluid displacement is a large volume difference between two adjacent pores, ΔV , which is illustrated on the right side of the graph. Initial and deformed geometry are shown on the left and right, respectively. All unit cells have a width of 60 mm and a ligament thickness of 2 mm between the pores. The pore diameters are: 28 mm \times 7 mm (black parallel ellipses), 28 mm \times 28 mm (red circles) and 42 mm \times 10.5 mm (blue perpendicular ellipses). The center to center distances are (vertical/horizontal): 30 mm/9 mm, 30 mm/30 mm and 60 mm/30 mm and the initial porosities are 57%, 68% and 19%, respectively.

buckling structure that stood out with large ΔV during numerical tests and test runs of fabrication as illustrated by the cast silicone structures in the introductory Fig. 1(c).

Moderate values of ΔV are expected and observed for elongated perpendicular pores that resemble a typical situation in rock formations. The volume difference in both pores increases with larger pre-compression and may thus be more pronounced in reservoir depths. Virtually no ΔV appears in circular pores, though. Despite their severe deformations, all pore volumes shrink equally and thus would not trigger any fluid exchange. The most drastic volume difference is eventually achieved for a regular array of parallel elliptical pores. After reaching the buckling threshold, neighboring elliptical pores close and open, respectively. This strong contrast in their volumetric evolution can trigger the largest fluid exchange among the basic geometries, which makes them ideal candidates to harness the local-flow mechanism for high attenuation. While these three architectures allow for a basic distinction of dry pore types, a more detailed parameter study will be performed for fluid-filled pores. We will focus on the parallel elliptical pores (black model in Fig. 4) in the following as a prototype model.

4. Harnessing buckling pores for local flow: parameter study of a prototype cell

The following parameter study demonstrates advantages and peculiarities of harnessing buckling pores for the local-flow mechanism. It uses the periodic silicone rubber-air prototype system described in Section 2 and Fig. 3 for variations of deformation state, geometry and materials. This discussion aims at the understanding of the processes with an emphasis on generalized findings before our conclusion, where we will compare the system specifically to values of alternative attenuation mechanisms.

4.1. Effect of pre-buckling on local-flow attenuation

Remarkably and specific to buckling structures, the attenuation can be switched on and off by modulation of the deformation state. No attenuation occurs for the homogeneous starting geometry and for moderate pre-compression states before buckling, see Fig. 5. Significant attenuation is however triggered at the critical pre-compression $\epsilon_{pre} = -6\%$ and further rises to a value in the range $0.3 < Q^{-1} < 0.4$. Employing a structural instability thus allows direct attenuation control by strain,

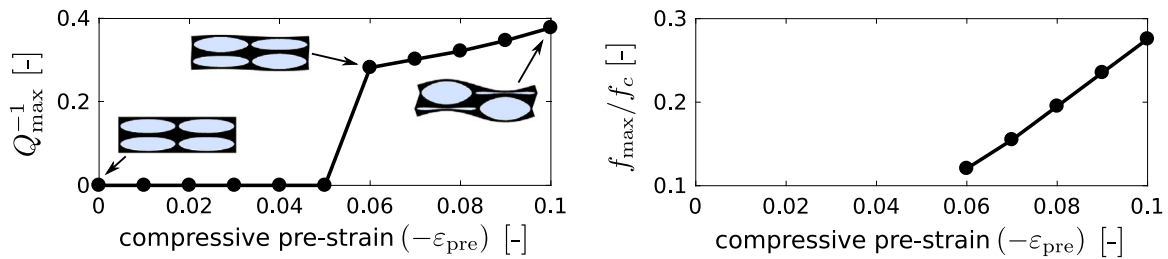


Fig. 5. Maximum attenuation given as the inverse quality factor Q_{\max}^{-1} and corresponding frequency f_{\max} normalized by the analytical approximation f_c in Eq. (10) at different compressive pre-strain. The frequency f_{\max} is only plotted if attenuation is larger than the numerical accuracy.

since local flow is activated by symmetry breaking. This stabilization of the local-flow effect with increasing pre-compression is moreover indicated by the course of the frequency of maximum attenuation determined from the simulations, f_{\max} . At higher pre-compression, f_{\max} rises towards the analytical approximation, f_c , and hence towards the situation of the idealized local-flow cell, Fig. 5. The following analyses are performed for a pre-compression of -10% , if not otherwise noted, which is slightly before the pores begin to close under contact.

4.2. Frequency tuning by fluid and pore connection

The attenuation of the periodic prototype structure shown in Fig. 3 has a maximum at 5.5 Hz. The corresponding frequency from the simulations, f_{\max} , scales directly with the analytical characteristic frequency, f_c , in Eq. (10). They are thus presented as a dimensionless ratio. Note that both frequencies do not match perfectly due to a different constant prefactor of their definitions, though. Additional deviation can occur if assumptions of the idealized local-flow cell are not fulfilled or if the local-flow mechanism is not fully triggered (Fig. 5, right). The frequency of maximum attenuation in natural rock formations can, for instance, deviate from the approximation because of their highly heterogeneous pore-size distribution or saturation (White et al., 1975; Dutta and Odé, 1979a,b; Quintal et al., 2011), which will lead to a broad frequency-dependent attenuation curve. The derived characteristic frequency f_c nevertheless provides a valid approximation for the present prototype system, because the latter involves only two pore sizes and a single time scale for the flow process. This allows to derive capable strategies for frequency tuning once buckling is triggered.

The fluid is a key element to control the frequency of maximum attenuation. A smaller fluid bulk elasticity K_f and larger viscosity η shift the response to lower frequencies. Note that strong control on the fluid bulk modulus can be achieved, for example, by injecting small amounts of gas in a liquid, allowing for a reduction of the fluid's bulk modulus by several orders of magnitude with only few percent of gas according to the Reuss average (Mavko et al., 2009). A second option to achieve attenuation at low frequencies is a reduction of permeability κ , that is, of the cross-sectional area A of the pore connections, e.g., by reducing the width or number of connecting channels. Increasing the connection length is another option but also probably a more intricate possibility considering fabrication. Harnessing the local character of the local-flow principle thus opens a number of possibilities to optimize low-frequency attenuation without changing the structure's size or shape.

4.3. Porosity and finite-size boundary effects

The key to maximized attenuation has been shown to be a geometry that is susceptible to deformations with opposite volume changes in neighboring pores, cf. Fig. 4. Buckling pores may trigger such substantial geometrical changes, but their efficiency depends on an optimal geometrical design. Regarding the pore size, 10% less porosity (or 5% smaller ellipse diameters, respectively) already reduce the attenuation

by more than 13%, see Fig. 6 (left). The optimum porosity of 57% has been used for the initial prototype geometry.

Turning the view to application of finite-size systems, they are often known to perform less ideally compared to a perfectly periodic cell. This is confirmed as an array of 2×2 pores does not show the desired asymmetric deformation at all because of the fixed boundaries of the present setup, see Fig. 6 (right). Buckling that is prone to local flow nevertheless evolves for larger structures and tends towards the periodic case for at least 6×6 pores. Larger structures up to 12×12 pores almost reach 80% of the periodic case or $Q^{-1} \approx 0.3$. The frequency of maximum attenuation can slightly drop due to the boundary influence to around 3 Hz. The scaling ability of the local-flow principle and modern printing or casting techniques of elastic structures thus support approaching the periodic attenuation by stacking of local-flow cells. It suffices to connect only pairs of neighboring pores.

4.4. Material combination and conflicting design goals

The material combination of solid and fluid shows a conflicting design goal that could not be anticipated from traditional local-flow theories or approximations such as Eqs. (8) and (10). In general, a soft structure should yield higher attenuation, which corresponds to minimizing static modulus c in Eq. (8). Less elastic energy is then stored during deformation and the ratio of dissipated to total energy is higher.

On one hand, raising the structural stiffness via the solid's Youngs modulus (or E_s/K_f , respectively) does diminish attenuation as expected, cf. the right slope of Q^{-1} in Fig. 9. A softer structural frame should be thus favorable. On the other hand, however, reducing the stiffness does not unconditionally increase attenuation as it starts to decrease again for very soft structures, cf. the left slope of Q^{-1} in Fig. 9. This can be explained only when analyzing the fluid-structure interaction on the pore scale. The simulations showed that buckling is not fully triggered in these cases. External loading cannot be transformed into the desired buckling mode if the solid is too compliant. The comparably rigid fluid hinders asymmetric buckling that is required for dissipative fluid exchange. The evolution of f_{\max} over E_s/K_f (Fig. 7) supports this finding. The frequency of maximum attenuation f_{\max} approaches the analytical characteristic frequency f_c only if the solid is stiff enough to impose the buckling mode upon the fluid.

Eventually, choosing the solid and fluid elastic moduli must be a careful compromise — elasticity must be just high enough to impose buckling and yet small enough to transform as much remaining energy as possible into dissipative flow. The peak ratio of $E_s/K_f = 10^2$ was therefore used as a starting material combination and motivated the corresponding silicone rubber-air prototype system.

4.5. Comparison with dissipation in natural rocks

The inverse quality factor of the presented structure exceeds largely that of natural squirt flow or local flow (Müller et al., 2010; Gurevich and Carcione, 2022; Dvorkin and Nur, 1993) due to its mechanical peculiarities. The static modulus is much lower, e.g., three orders of magnitude smaller than in sandstone (Wang, 2000), see the values for

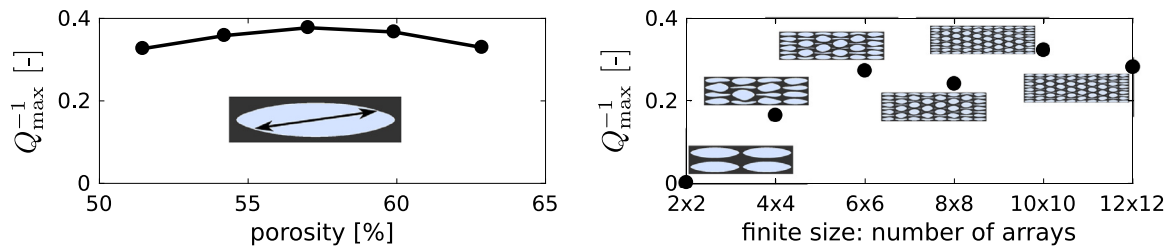


Fig. 6. Maximum attenuation given as the inverse quality factor Q_{\max}^{-1} of the prototype structure for different porosities of a periodic cell and for non-periodic structures of finite size at -10% pre-compression.

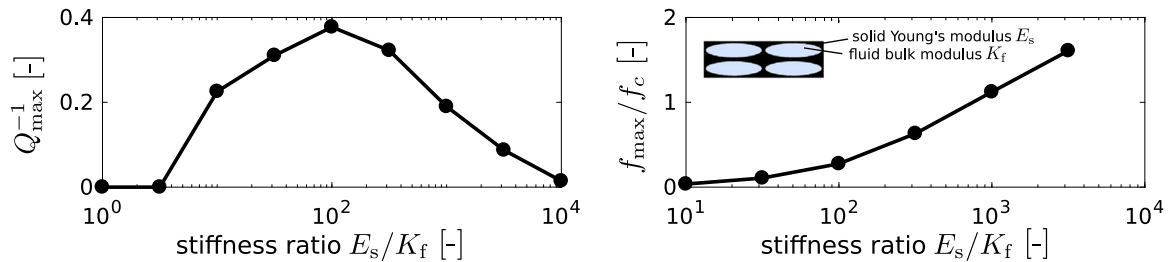


Fig. 7. Maximum attenuation given as the inverse quality factor Q_{\max}^{-1} and corresponding frequency f_{\max} normalized by f_c in Eq. (10) of the prototype structure for different stiffness ratios of solid Young's modulus to fluid bulk modulus E_s/K_f .

the periodic prototype structure in Fig. 8(a). One reason for that low modulus is the soft bulk solid material in the range of soft rubbers with a shear modulus of 3.45 MPa and a Young's modulus of 10 MPa in the reference setting. Variations of the duplicating silicone used for the samples in Fig. 1 (Zhermack Elite Double) can even reach elastic moduli below 1 MPa (Babae et al., 2015; Kurzeja and Tang, 2015). Additionally, the high porosity reduces the effective stiffness of the dry structure even further to the order of 1 MPa. The deformation modes are mainly related to shape changes and thus to the shear modulus of the bulk material. Buckling further reduces the stiffness, which is clearly noticeable but not vital for the aim of maximized attenuation (compare the moduli between the unbuckled and the buckled state in Fig. 8(a)). Attenuation is already high in the post-buckling regime, the buckling transition itself is not required. The main purpose of the instability is to trigger a deformation mode beforehand, which allows for local flow. It is the dynamic perturbation that is triggering local flow. Utilizing the strongly non-linear buckling transition can offer an increased effect but exceeds the scope of the present focus on linear behavior and the comparison with typically wave-induced dispersion. The fluid contributes to both the static modulus and the dynamic modulus. The dynamic influence is however amplified due to the large volume exchange $\Delta V_1 - \Delta V_2$ between the pores. Considering the postbuckling regime ($-0.06 > \varepsilon_{\text{pre}} \geq -0.10$), yields relative volume changes of two adjacent pores of $\Delta V_1/V_0 = -33\%$ and $\Delta V_2/V_0 = +19\%$, cf. Fig. 4. The total relative volume change of both pores is $0.5(\Delta V_1 + \Delta V_2)/V_0 = -7\%$ and thus approximately in the same order of the compressive strain of $\Delta \varepsilon = -4\%$. It is the total relative volume exchange between the pores that determines the dissipative effect, though. This exchange amounts to $0.5(\Delta V_1 - \Delta V_2)/V_0 = -26\%$. This strengthens the fluid's effect on the dynamic modulus, despite the relatively small stimulating strain and fluid's bulk modulus.

The large attenuation effect of the presented structures can also be observed in the strong dispersion of the inverse quality factor and phase velocity, see Fig. 8(b). The phase velocity starts at 40 m/s in the low-frequency limit and reaches 58 m/s at higher frequencies, underlining the large change in the associated stiffnesses. It has been determined from the complex modulus $M(f)$ and the averaged density of the mixture $\rho^{\text{mixture}} = 502 \text{ kg/m}^3$ (based on a rubber bulk density of 1050 kg/m^3 and 10% pre-compression). The phase velocity dispersion

is dictated by the Kramers–Krönig relations and was calculated by the formula in Ursin and Toverud (2002) as

$$v_{\text{phase}}(f) = \sqrt{\frac{2|M|^2}{\rho^{\text{mixture}}(M_{\text{real}} + |M|)}}. \quad (13)$$

It should be noted that a homogenized treatment of the unit cell's density and effective stiffness is supported by scale separation, because the relevant wave length is in the order of 10 m and thus much larger than the characteristic pore size. Effects such as scattering or resonance band gaps are not accounted for, however, and will of course superpose the predicted behavior at higher frequency regimes. Moreover, the FFT evaluation matches the fit to an SLS-rheology very well (compare the Q^{-1} predictions in Fig. 8(b)), which supports the assumption of a single time scale in the architected structure of regular arrays. The complex microstructure in natural materials, in contrast, yields a more complex dispersion and time scales involved (Müller et al., 2010).

5. Conclusions and comparison with other attenuation mechanisms

We have shown that buckling pores can allow for substantial attenuation at low frequencies. First, we examined that elliptical pores amplify the fluid exchange that is required for dissipation based on the principle of local flow as observed in fluid-saturated rocks. Second, we showed that the corresponding frequencies can be reduced not only by geometric properties such as permeability or pore sizes but also by the viscosity and compliance of fluids or fluid mixtures. Inverse quality factors up to 0.38 at 5.5 Hz (periodic) and 0.30 at 3.0 Hz (finite size) are numerically observed for air-filled elliptical pores in soft rubber under 10% pre-compression. Attenuation is directly controlled by the state of pre-compression via asymmetric pore buckling, which allows for dissipative flow.

The mechanism studied along with the presented prototype structure stands out compared to other attenuating mechanisms especially in terms of the inverse quality factor in the low-frequency regime (Fig. 9). It exceeds Biot flow and natural local flow in saturated rock, which constituted the starting point of the present study. Also polystyrene, PMMA, polyester, plastic foam, rubber, shape memory polymers and damage in composites do not reach that performance at comparable frequencies. Pure polyurethane, polypropylene, PVC and fracture flow

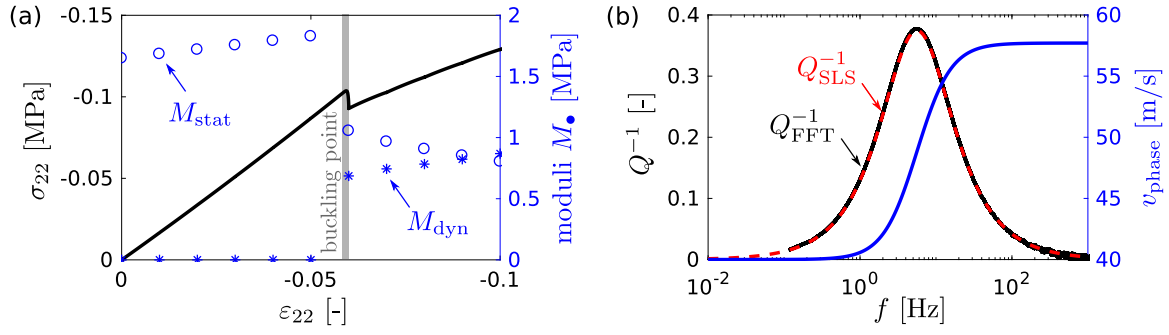


Fig. 8. (a) Quasi-static stress–strain response with static and dynamic moduli at selected deformation states of the periodic prototype structure. (b) Dispersion relations of the local-flow effect at 10% precompression of the periodic structure. The inverse quality factor is shown as determined from an FFT and from an SLS-fit.

without finite-size effects also do not achieve the Q^{-1} -value of buckling-induced local flow, while attenuation in foams of comparable size starts at much larger frequencies. Candidates rivaling the presented prototype example in the low-frequency range are based on heavy-weight solids that also rely on microscopic shearing of viscous components, e.g., asphalt and concrete. Also note that the presented results can be superposed by other, potentially dissipative effects in the entire frequency spectrum such as solid viscosity, resonance band gaps or scattering.

Local flow in buckling pores opens a new avenue to tune low-frequency attenuation by contrasting existing mechanisms that were designed for complementary operation purposes such as broader frequency bands, electronic band-gap control or fluid-free attenuation. Its unique and important features can be summarized as:

- porous, light-weight structure
- maximized attenuation at seismic frequencies by buckling
- pore fluid properties changed to tune attenuation frequency
- scalable and small unit cells
- attenuation can be switched on and off reversibly by pre-compression

Due to their intentionally low stiffness, nevertheless, the presented buckling structures cannot bear large weights themselves and attenuation depends on the deformation direction. They can hence perform as ideal candidates to support existing constructions as deformation-controlled low-frequency dampers. Their attenuation works in a configured orientation, the pores show reversible folding capabilities and can be saturated with different fluids. Future exploration of three-dimensional examples and laboratory experiments will take the promising design in this fundamental feasibility study closer to devising light-weight, flexible materials that employ dissipative flow on a local scale.

Declaration of competing interest

The authors declare that they have no known competing financial interests or personal relationships that could have appeared to influence the work reported in this paper.

Data availability

The Python control files for performing an Abaqus simulation of a prototype finite size structure and Matlab postprocessing files are provided.

Acknowledgments

PK gratefully acknowledges support from German Research Foundation (Deutsche Forschungsgemeinschaft) grants KU 3351/1-1 and KU 3351/2-1. BQ gratefully acknowledges support from the Swiss National

Science Foundation (Schweizerischer Nationalfonds zur Förderung der Wissenschaftlichen Forschung) grants 172691 and 212730. Insightful inputs on the manuscript and valuable discussions with Katia Bertoldi, Tal Cohen and Marcel Frehner are thankfully acknowledged.

Appendix A. Linear solution of pressure relaxation between two pores

In the following, we will derive the inverse quality factor for two connected fluid-filled pores inside an elastically deformable host matrix comprising an idealized unit cell for local flow. The properties of the two pores are indicated by subscripts $j \in \{1, 2\}$. Initial values are indicated by a subscript 0, while the initial pore volumes V_0 and pore fluids are assumed to be equal. The analysis is concerned with fully linear perturbations.

A strain perturbation $\Delta\epsilon$ shall be applied on the cell, e.g., a plane-strain compression in the present case. The corresponding modulus M can be split into a volumetric part M^{vol} including fluid-pressure changes and a remaining part M^{extra} related to extra stresses solely captured by the solid frame. Starting with the volumetric change of the fluid-filled cell (ΔV^{cell}), it is first divided into a volume change of the fluid (ΔV^{f}) and two volume changes of the solid due to fluid pressure ($\Delta V^{\text{p,s}}$) and due to the extra pressure in the frame ($\Delta V^{\text{extra,s}}$), respectively,

$$\Delta V^{\text{cell}} = \Delta V^{\text{f}} + \Delta V^{\text{p,s}} + \Delta V^{\text{extra,s}} = \Delta V^{\text{f}} - \Delta p \frac{V_0^{\text{f}}}{K_s} \frac{1 - \phi_0}{\phi_0} + (1 - \beta) \Delta V^{\text{cell}}.$$

The solid deformation induced by fluid pressure (the second term in the above equation) is related to a factor based on initial porosity of the cell $\phi_{j,0}^{\text{cell}} = V_0^{\text{f}} / (V_0^{\text{f}} + V_0^{\text{s}})$ and the bulk modulus of the solid bulk material K_s (not to be confused with the bulk modulus of the porous solid frame). It results from the volumetric compression of the solid by pressure as $\Delta V^{\text{p,s}} / V_0^{\text{s}} = -\Delta p / K_s$ and reformulation via the porosity.

The proportionality factor β in the last term of the above equation determines how an external load is distributed between fluid pressure (as discussed above) and extra stresses. See, for instance, (Ortiz et al., 2013) and (Vinci et al., 2014) and the Biot-Willis coefficient for dry structures in poroelasticity for more details on the distribution between fluid pressure and extra stresses (Mavko et al., 2009; Wang, 2000). In the present case, this volumetric contribution of extra stresses in the frame will be considered implicitly in the static modulus M^{extra} .

The solid frame is furthermore assumed to show a purely elastic, rate-independent response and to be more compliant than the bulk solid. This accordingly yields to slow wave propagation speeds in highly porous, soft structures (Kurzeja and Tang, 2015). As one result, the so-called rigid-grain approach (Steeb, 2010), with $K_s \rightarrow \infty$, is a reasonable assumption compared to the stiffness of the fluid and the porous frame. Eventually, in the present case of gas-filled soft structures, volumetric changes are dominated by compression of the pore fluid. It will be used frequently in the following derivation to simplify the relationships.

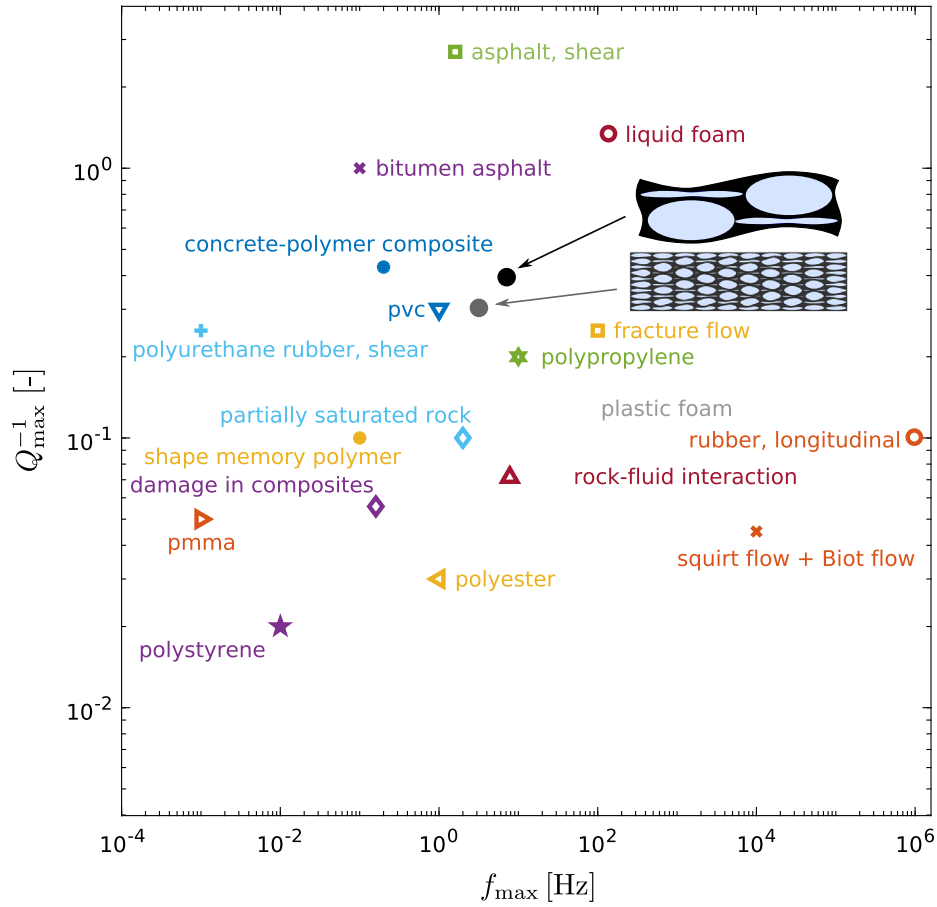


Fig. 9. Comparison between the presented prototype structure (periodic and finite size at pre-compression of -10% indicated by sketches) and other attenuation mechanisms. Literature data is shown as characteristic maximum peaks at the lowest frequency reported and taken from: Pritz (1994, plastic foam), Pritz (1998, rubber, longitudinal), Kazakevičiūtė-Makovska et al. (2014, shape memory polymer), Schüller et al. (2013, bitumen asphalt), Dickinson and Witt (1974, asphalt, shear), Quintal et al. (2011, partially saturated rock), Pujol et al. (1998, rock-fluid interaction), Herbert et al. (2008, PVC), Gibson and Ashby (1999, PMMA, polyester, polystyrene, polypropylene), Mott et al. (2002, polyurethane rubber, shear), Pierre et al. (2014, liquid foam), Chung (2003, concrete-polymer composite), Dvorkin and Nur (1993, squirt flow + Biot flow), Vinci et al. (2014, fracture flow) and Junker and Kochmann (2017, damage in composites).

T_j is an auxiliary proportionality factor that defines the pressure-induced volume change of each cavity under compression with respect to strain changes as

$$T_j = \frac{\Delta V_j^p}{\Delta \epsilon} = \frac{\Delta V_j^f + \Delta V_j^{p,s}}{\Delta \epsilon} \quad K_f \ll K_s \quad \frac{\Delta V_j^f}{\Delta \epsilon}$$

Local flow further requires fluid mass exchange \dot{m}_j^f between the two cavities that can be approximated in the linear case by

$$-\dot{m}_2^f = \dot{m}_1^f = \Delta V_1^f \rho_0^f + V_{1,0}^f \Delta \rho_1^f = \rho_0 \gamma (\Delta p_2 - \Delta p_1), \quad \gamma = \frac{\kappa A}{l \eta}$$

To complete the set of equations, we use the conservation of mass and the equation of state for barotropic fluids in the linear form as

$$\Delta V_1^f \rho_0^f + V_{1,0}^f \Delta \rho_1^f + \Delta V_2^f \rho_0^f + V_{2,0}^f \Delta \rho_2^f = 0 \quad \text{and} \quad \Delta \rho_j^f = \frac{\rho_0^f}{K_f} \Delta p_j$$

The previously stated equations can then be finally combined to the partial differential equation

$$\Delta p_1 + \Delta p_1 [\chi (S_1^{\text{eff}} + S_2^{\text{eff}})] + \Delta \epsilon [T_1 S_1^{\text{eff}}] + \Delta \epsilon [\chi S_1^{\text{eff}} S_2^{\text{eff}} (T_1 + T_2)] = 0.$$

Therein, we introduced the effective cavity stiffness

$$S_j^{\text{eff}} = \frac{K_f}{V_{j,0}^f} \frac{K_s \phi_{j,0}}{K_s \phi_{j,0} + K_f (1 - \phi_{j,0})} \quad K_f \ll K_s \quad \frac{K_f}{V_{j,0}^f},$$

which is a combination of fluid and solid bulk modulus, K_f and K_s , and weighted by the initial cavity volume V_0^f and initial porosity of the entire unit cell $\phi_{j,0}^{\text{cell}} = V_0^f / (V_0^f + V_0^s)$.

Combining these definitions and the relationships introduced for the material description in 2.1 into the mass balance, yields the governing relationship between the pressure change in the first pore (Δp_1) and the external strain perturbation ($\Delta \epsilon$) in the form of a partial differential equation

$$\begin{aligned} \Delta p_1 + \Delta p_1 \left[\gamma 2 \frac{K_f}{V_0} \frac{K_s \phi_0 / 2}{K_s \phi_0 / 2 + K_f (1 - \phi_0 / 2)} \right] \\ + \Delta \epsilon \left[\frac{K_f}{V_0} \frac{K_s \phi_0 / 2}{K_s \phi_0 / 2 + K_f (1 - \phi_0 / 2)} \frac{\Delta V_1}{\Delta \epsilon} \right] \\ + \Delta \epsilon \left[\gamma \left(\frac{K_s \phi_0 / 2}{K_s \phi_0 / 2 + K_f (1 - \phi_0 / 2)} \right)^2 \frac{\Delta V_1 + \Delta V_2}{\Delta \epsilon} \right] = 0. \end{aligned}$$

The rigid-grain approach yields Eq. (6) for $K_s \rightarrow \infty$.

As a next step, we derive the dynamic modulus for the fluid's pressure-induced response from a stress relaxation problem. Assuming an instantaneous strain perturbation $\Delta \epsilon = \hat{\epsilon} H(t)$ with $H(t)$ being the unit step function, the instantaneous volume changes are $\Delta V_j = (\Delta V_j / \Delta \epsilon) \hat{\epsilon} H(t)$. This yields the following pressure solution for $t > 0$ and $j \in \{1, 2\}$

$$\begin{aligned} \Delta p_j(t) = (p_{j,\text{start}} - p_{\text{end}}) e^{-2\pi f_c t} + p_{\text{end}}, \quad p_{j,\text{start}} = -\frac{\Delta V_j}{\Delta \epsilon} \frac{V_0}{K_f} \hat{\epsilon}, \\ p_{\text{end}} = -\frac{\Delta V_1 + \Delta V_2}{2 \Delta \epsilon} \frac{V_0}{K_f} \hat{\epsilon} \end{aligned}$$

in the time domain and

$$\Delta \epsilon(f) = \hat{\epsilon} \frac{1}{2} \left(\frac{1}{\pi i f} + \delta(f) \right), \quad \Delta p_j(f) = \frac{(p_{j,\text{start}} - p_{\text{end}})}{2\pi f_c + 2\pi i f}$$

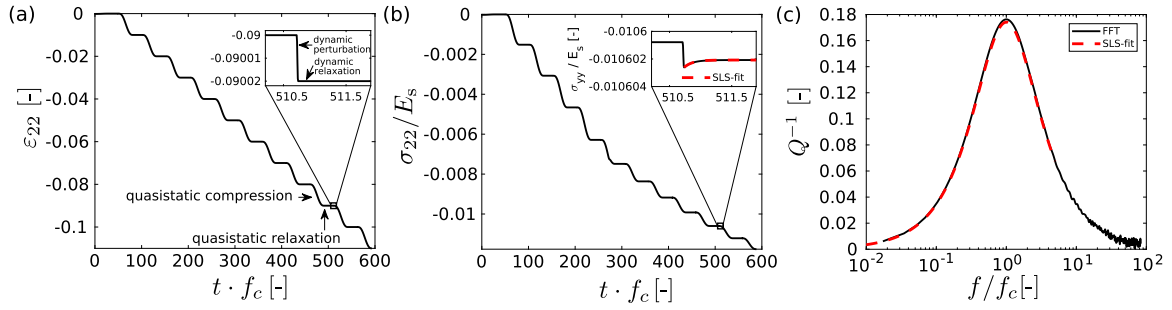


Fig. B.10. (a) Strain evolution and (b) stress response over time during intermittent quasi-static pre-compression and dynamic perturbation for the example of the 12×12 finite prototype structure. (c) Inverse quality factor over frequency as calculated from an FFT analysis and an SLS-fit, respectively, for the same structure.

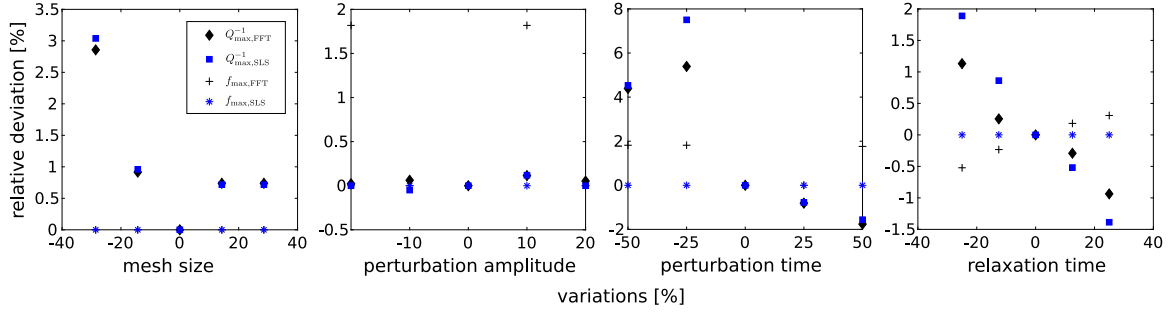


Fig. C.11. Sensitivity study of mesh size, perturbation amplitude, perturbation time and relaxation time of the dynamic step for the example of the periodic structure under pre-compression of $\epsilon_{pre} = -10\%$. Shown are values of maximum inverse quality factor and the associated frequency derived from an FFT evaluation and from an SLS fit.

$$+ p_{end} \frac{1}{2} \left(\frac{1}{\pi i f} + \delta(f) \right)$$

in the frequency domain with $i = \sqrt{-1}$, $\delta(f)$ being the Dirac delta distribution and the characteristic frequency f_c defined in (10).

The solution describes a simple relaxation process that is similar to the rheology of a Standard Linear Solid (SLS)-model (also known as the Zener-model) (de Haan and Sluimer, 2001). This allows us to derive the frequency-dependent moduli from the energy derivative $\partial^2 \Delta(p_1 V_1 + p_2 V_2) / \partial \epsilon^2$ for the fluid pressure-induced deformation. Adding them to the purely elastic extra modulus of the frame yields the static and dynamic moduli for the entire unit cell as given in Eq. (7).

The frequency-dependent dynamic modulus and inverse quality factor for this case of an SLS-rheology read

$$M(f) = M_{stat} + M_{dyn} \left(\frac{(f/f_c)^2}{1 + (f/f_c)^2} + i \frac{(f/f_c)}{1 + (f/f_c)^2} \right),$$

$$Q^{-1}(f) = \left| \frac{\Im(M)}{\Re(M)}(f) \right| = \frac{(f/f_c)(M_{dyn}/M_{stat})}{1 + (f/f_c)^2 (1 + (M_{dyn}/M_{stat}))}.$$

At the frequency of maximum attenuation, $f_{max} = f_c / \sqrt{1 + (M_{dyn}/M_{stat})}$, the inverse quality factor peaks at the value of $Q_{max}^{-1} = 0.5 (M_{dyn}/M_{stat}) / \sqrt{1 + (M_{dyn}/M_{stat})}$. Inserting the specific static and dynamic moduli of (7) finally yields the inverse quality factor in terms of volume exchange, characteristic frequency and static stiffness contribution in Eqs. (8)–(11).

Appendix B. Calculation of the inverse quality factor from stress response

The inverse quality factor is determined by a Fast Fourier Transformation of the integrated stress and strain rates of the dynamic perturbation response, $\Delta\hat{\sigma}(f)$ and $\Delta\hat{\epsilon}(f)$, as (Quintal et al., 2011)

$$Q^{-1}(f) = - \frac{\text{Im}(\Delta\hat{\sigma}(f)/\Delta\hat{\epsilon}(f))}{\text{Re}(\Delta\hat{\sigma}(f)/\Delta\hat{\epsilon}(f))}$$

In addition to an evaluation via FFT, the normal stress perturbation in vertical direction $\delta\sigma(t)$ is monitored and fitted to the response of an

SLS rheology with

$$\Delta\sigma_{SLS}(t) = M_{stat} \Delta\epsilon + M_{dyn} \Delta\epsilon e^{-2\pi f_c t}.$$

The static modulus, the dynamic modulus and the characteristic frequency then allow to double check the frequency-dependent inverse quality factor (Ursin and Toverud, 2002; O'Connell and Budiansky, 1977).

The results of the FFT analysis and the SLS fit show a very good match, see Fig. B.10 for an example and Fig. C.11 of the sensitivity study below. Significant deviations were only observed when no local flow is triggered and attenuation falls in the regime of numerical uncertainties or for compression states that exceed closure of the pores. These states were accordingly excluded from attenuation measurements and discussion. A single SLS-fit is not as feasible for finite size structures, since the pore deformation deviated in the boundary region and comprise a broader, more complex frequency spectrum — yet a consistent single peak could be clearly identified. The match of FFT and SLS approach supports the analytical solution used in Eqs. (8) and (10) and also indicates the choice of the correct time scale.

Appendix C. Sensitivity study

A comprehensive sensitivity study of the initial system is employed to evaluate the values of maximum inverse quality factor and the associated frequency, see Fig. C.11. Mesh independence is asserted by a mesh convergence study. The perturbation amplitude was chosen as a compromise between numerical sensitivity and linearity in the perturbation step. The variations of perturbation and relaxation time are tested for large variations to explore the limits of too small time scales (yielding inertia effects and incomplete relaxation) and too large time scales (yielding quasistatic creep) that exceed the scope of this work. The time scale of loading for linear perturbation ($\approx 0.035 f_c^{-1}$) has been determined from iterative testing for the combination of structural stiffness to viscosity effects at hand, which is in agreement with observations of local flow in natural materials. For moderate variations of the numerical setting up to $\pm 5\%$, all expected deviations remain in the

regime of single-digit percentage. Exceptions appear where numerical uncertainties dominate or where evaluation is not feasible. Respective values have consequently been omitted, for example, characteristic frequencies for unbuckled structures.

Appendix D. Supplementary data

Supplementary material related to this article can be found online at <https://doi.org/10.1016/j.ijsolstr.2023.112508>.

References

- Adelinet, M., Fortin, J., Guéguen, Y., 2011. Dispersion of elastic moduli in a porous-cracked rock: Theoretical predictions for squirt-flow. *Tectonophysics* 503, 173–181. <http://dx.doi.org/10.1016/j.tecto.2010.10.012>.
- Alkhimenkov, Y., Quintal, B., 2022a. An accurate analytical model for squirt flow in anisotropic porous rocks - part 1: Classical geometry. *Geophysics* 87, MR85–MR103. <http://dx.doi.org/10.1190/geo2021-0229.1>.
- Alkhimenkov, Y., Quintal, B., 2022b. An accurate analytical model for squirt flow in anisotropic porous rocks - part 2: Complex geometry. *Geophysics* 87, MR291–MR302. <http://dx.doi.org/10.1190/geo2022-0143.1>.
- Babae, S., Wang, P., Bertoldi, K., 2015. Three-dimensional adaptive soft phononic crystals. *J. Appl. Phys.* 117. <http://dx.doi.org/10.1063/1.4923032244903>.
- Bertoldi, K., Boyce, M.C., 2008a. Mechanically-triggered transformations of phononic band gaps in periodic elastomeric structures. *Phys. Rev. B* 77, 052105. <http://dx.doi.org/10.1103/PhysRevB.77.052105>.
- Bertoldi, K., Boyce, M.C., 2008b. Wave propagation and instabilities in monolithic and periodically structured elastomeric materials undergoing large deformations. *Phys. Rev. B* 78, 184107. <http://dx.doi.org/10.1103/PhysRevB.78.184107>.
- Bertoldi, K., Boyce, M.C., Deschanel, S., Prange, S.M., Mullin, T., 2008. Mechanics of deformation-triggered pattern transformations and superelastic behavior in periodic elastomeric structures. *J. Mech. Phys. Solids* 56, 2642–2668. <http://dx.doi.org/10.1016/j.jmps.2008.03.006>.
- Borgomano, J.V.M., Pimienta, L.X., Fortin, J., Guéguen, Y., 2019. Seismic dispersion and attenuation in fluid-saturated carbonate rocks: Effect of microstructure and pressure. *J. Geophys. Res.: Solid Earth* 124, 12498–12522. <http://dx.doi.org/10.1029/2019JB018434>.
- Brajanovski, M., Gurevich, B., Schoenberg, M., 2005. A model for P-wave attenuation and dispersion in a porous medium permeated by aligned fractures. *Geophys. J. Int.* 163, 372–384. <http://dx.doi.org/10.1111/j.1365-246X.2005.02722.x>.
- Carlstedt, D., Runesson, K., Larsson, F., Tu, V., Jänicke, R., Asp, L.E., 2022. Computational modelling of structural batteries accounting for stress-assisted convection in the electrolyte. *Int. J. Solids Struct.* 238, 111343. <http://dx.doi.org/10.1016/j.ijsolstr.2021.111343>.
- Chapman, S., Borgomano, J.V.M., Yin, H., Fortin, J., Quintal, B., 2019. Forced oscillation measurements of seismic wave attenuation and stiffness moduli dispersion in glycerine-saturated Berea sandstone. *Geophys. Prospect.* 67, 956–968. <http://dx.doi.org/10.1111/1365-2478.12710>.
- Chevillotte, F., Perrot, C., Guillon, E., 2013. A direct link between microstructure and acoustical macro-behavior of real double porosity foams. *J. Acoust. Soc. Am.* 134, 4681–4690. <http://dx.doi.org/10.1121/1.4824842>.
- Chung, D.D.L., 2001. Review: Materials for vibration damping. *J. Mater. Sci.* 36, 5733–5737. <http://dx.doi.org/10.1023/A:1012999616049>.
- Chung, D.D.L., 2003. Structural composite materials tailored for damping. *J. Alloys Compd.* 355, 216–223. <http://dx.doi.org/10.1016/S0925-8388>.
- Ciz, R., Saenger, E.H., Gurevich, B., 2006. Pore scale numerical modeling of elastic wave dispersion and attenuation in periodic systems of alternating solid and viscous fluid layers. *J. Acoust. Soc. Am.* 120, 642–648. <http://dx.doi.org/10.1121/1.2216687>.
- Cohen, T., Kurzeja, P., Bertoldi, K., 2017. Architected squirt-flow materials for energy dissipation. *J. Mech. Phys. Solids* 109, 22–33. <http://dx.doi.org/10.1016/j.jmps.2017.08.003>.
- Collet, O., Gurevich, B., 2016. Frequency dependence of anisotropy in fluid saturated rocks - part i: aligned cracks case. *Geophys. Prospect.* 64, 1067–1084. <http://dx.doi.org/10.1111/1365-2478.12384>.
- Danielsson, M., Parks, D.M., Boyce, M.C., 2002. Three-dimensional micromechanical modeling of voided polymeric materials. *J. Mech. Phys. Solids* 50, 351–379.
- de Haan, Y.M., Sluimer, G.M., 2001. Standard linear solid model for dynamic and time dependent behaviour of building materials. *HERON* 46, 49–76.
- Dickinson, E.J., Witt, H.P., 1974. The dynamic shear modulus of paving asphalt as a function of frequency. *J. Rheol.* 18, 591–606. <http://dx.doi.org/10.1122/1.549349>.
- Dos Reis, F., Karathanasopoulos, N., 2022. Inverse metamaterial design combining genetic algorithms with asymptotic homogenization schemes. *Int. J. Solids Struct.* 250, 111702. <http://dx.doi.org/10.1016/j.ijsolstr.2022.111702>.
- Dutta, N.C., Odé, H., 1979a. Attenuation and dispersion of compressional waves in fluid-filled porous rocks with partial gas saturation (white model), Part I: Biot theory. *Geophysics* 44, 1777–1788. <http://dx.doi.org/10.1190/1.1440938>.
- Dutta, N.C., Odé, H., 1979b. Attenuation and dispersion of compressional waves in fluid-filled porous rocks with partial gas saturation (White model), Part II: Results. *Geophysics* 44, 1789–1805. <http://dx.doi.org/10.1190/1.1440939>.
- Dvorkin, J., Nolen-Hoeksema, R., Nur, A., 1994. The squirt-flow mechanism: Macroscopic description. *Geophysics* 59, 428–438. <http://dx.doi.org/10.1190/1.1443605>.
- Dvorkin, J., Nur, A., 1993. Dynamic poroelasticity: A unified model with the squirt and the Biot mechanisms. *Geophysics* 58, 524–533. <http://dx.doi.org/10.1190/1.1443435>.
- Esposito, L., Minutolo, V., Fraldi, M., Sacco, E., 2022. Stress peaks, stiffening and back-flow in bilayer poro-elastic metamaterials. *Int. J. Solids Struct.* 236–237, 111334. <http://dx.doi.org/10.1016/j.ijsolstr.2021.111334>.
- Geli, L., Piau, J.M., Dziak, R., Maury, V., Fitzenz, D., Coutellier, Q., Henry, P., Broseta, D., Steele-MacInnis, M., Driesner, T., 2014. Seismic precursors linked to highly compressible fluids at oceanic transform faults. *Nat. Geosci.* 7, 757–761. <http://dx.doi.org/10.1038/ngeo2244>.
- Gibson, L., Ashby, M., 1999. *Cellular Solids: Structure and Properties*. Cambridge University Press.
- Graesser, E.J., Wong, C.R., 1991. *The Relationship of Traditional Damping Measures for Materials with High Damping Capacity*. Technical Report. DTRC-SME-91/05, David Taylor Research Center.
- Gurevich, B., Carcione, J.M., 2022. Attenuation and Dispersion of Elastic Waves in Porous Rocks: Mechanisms and Models. Society of Exploration Geophysicists. <http://dx.doi.org/10.1190/1.9781560803911>.
- Gurevich, B., Makarynska, D., De Paula, O.B., Pervukhina, M., 2010. A simple model for squirt-flow dispersion and attenuation in fluid-saturated granular rocks. *Geophysics* 75, N109–N120. <http://dx.doi.org/10.1190/1.3509782>.
- Hedayatrasa, S., Kersemans, M., 2022. 3D intra-cellular wave dynamics in a phononic plate with ultra-wide bandgap: attenuation, resonance and mode conversion. *Smart Mater. Struct.* 31, 035010. <http://dx.doi.org/10.1088/1361-665x/ac4d65>.
- Herbert, E.G., Oliver, W.C., Pharr, G.M., 2008. Nanoindentation and the dynamic characterization of viscoelastic solids. *J. Phys. D: Appl. Phys.* 41, 074021. <http://dx.doi.org/10.1088/0022-3727/41/7/074021>.
- Hudleston, P.J., Treagus, S.H., 2010. Information from folds: A review. *J. Struct. Geol.* 32, 2042–2071. <http://dx.doi.org/10.1016/j.jsg.2010.08.011>.
- Jänicke, B., Steeb, H., 2015. Numerical homogenization of mesoscopic loss in poroelastic media. *Eur. J. Mech. A Solids* 49, 382–395. <http://dx.doi.org/10.1016/j.euromechsol.2014.08.011>.
- Jian, Y., Tang, L., Hu, G., Wang, Y., Aw, K.C., 2022. Adaptive genetic algorithm enabled tailoring of piezoelectric metamaterials for optimal vibration attenuation. *Smart Mater. Struct.* 31, 075026. <http://dx.doi.org/10.1088/1361-665x/ac775d>.
- Jones, T.D., 1986. Pore fluids and frequency-dependent wave propagation in rocks. *Geophysics* 51, 1939–1953. <http://dx.doi.org/10.1190/1.1442050>.
- Junker, P., Kochmann, D.M., 2017. Damage-induced mechanical damping in phase-transforming composites materials. *Int. J. Solids Struct.* 113, 132–146. <http://dx.doi.org/10.1016/j.ijsolstr.2017.01.040>.
- Kazakevičiūtė-Makovska, R., Özarmut, A.O., Steeb, H., 2014. Characterization of shape memory polymer estane by means of dynamic mechanical thermal analysis technique. *Smart Mater. Res.* 9. <http://dx.doi.org/10.1155/2014/250258>, 2014.
- Kurzeja, P.S., Steeb, H., 2014a. Variational formulation of oscillating fluid clusters and oscillator-like classification, I. Theory. *Phys. Fluids* 26, 042106. <http://dx.doi.org/10.1063/1.4871486>.
- Kurzeja, P.S., Steeb, H., 2014b. Variational formulation of oscillating fluid clusters and oscillator-like classification, II. Numerical study of pinned liquid clusters. *Phys. Fluids* 26, 042107. <http://dx.doi.org/10.1063/1.4871489>.
- Kurzeja, P., Tang, J., 2015. Wave dispersion in highly deformable, fluid-filled structures: Numerical and experimental study of the role of solid deformation and inertia. In: *Proceedings of Meetings on Acoustics*. p. 25. <http://dx.doi.org/10.1121/2.0000374065001>.
- Lu, T.J., Hess, A., Ashby, M.F., 1999. Sound absorption in metallic foams. *J. Appl. Phys.* 85, 7528–7539. <http://dx.doi.org/10.1063/1.370550>.
- Madonna, C., Quintal, B., Fehner, M., Almqvist, B.S.G., Tisato, N., Pistone, M., Marone, F., Saenger, E.H., 2013. Synchrotron-based x-ray tomographic microscopy for rock microstructure investigations. *Geophysics* 78, D53–D64. <http://dx.doi.org/10.1190/GEO2012-0113.1>, (used image B14_0815.rec.16 bit.tif downloaded on 25 2022 from <https://rockphysics.org/downloads>).
- Mavko, G., Mukerji, T., Dvorkin, J., 2009. *The Rock Physics Handbook: Tools for Seismic Analysis of Porous Media*, second ed. Cambridge University Press.
- Mavko, G., Nur, A., 1975. Melt squirt in the asthenosphere. *J. Geophys. Res.* 80, 1444–1448. <http://dx.doi.org/10.1029/JB080i011p01444>.
- Miller, S.A., 2002. Properties of large ruptures and the dynamical influence of fluids on earthquakes and faulting. *J. Geophys. Res.: Solid Earth* 107, ESE 3–ESE 3–13. <http://dx.doi.org/10.1029/2000JB000032>.
- Mott, P.H., Roland, C.M., Corsaro, R.D., 2002. Acoustic and dynamic mechanical properties of a polyurethane rubber. *J. Acoust. Soc. Am.* 111, 2753–2764. <http://dx.doi.org/10.1121/1.1459465>.
- Müller, T.M., Gurevich, B., Lebedev, M., 2010. Seismic wave attenuation and dispersion resulting from wave-induced flow in porous rocks - a review. *Geophysics* 75, 75A147–75A164. <http://dx.doi.org/10.1190/1.3463417>.

- O'Connell, R.J., Budson, B., 1977. Viscoelastic properties of fluid-saturated cracked solids. *J. Geophys. Res.* 82, 5719–5735. <http://dx.doi.org/10.1029/JB082i036p05719>.
- Ogden, R.W., 1997. *Non-Linear Elastic Deformations*. Courier Corporation.
- Ortiz, A., Jung, R., Renner, J., 2013. Two-dimensional numerical investigations on the termination of bilinear flow in fractures. *J. Geophys. Res.: Solid Earth* 4, 331–345. <http://dx.doi.org/10.5194/se-4-331-2013>.
- Overvelde, J.T.B., Shan, S., Bertoldi, K., 2012. Compaction through buckling in 2d periodic, soft and porous structures: Effect of pore shape. *Adv. Mater.* 24, 2337–2342. <http://dx.doi.org/10.1002/adma.201104395>.
- Pierre, J., Dollet, B., Leroy, V., 2014. Resonant acoustic propagation and negative density in liquid foams. *Phys. Rev. Lett.* 112, 148307. <http://dx.doi.org/10.1103/PhysRevLett.112.148307>.
- Pimienta, L., Fortin, J., Guéguen, Y., 2015a. Bulk modulus dispersion and attenuation in sandstones. *Geophysics* 80, D111–D127. <http://dx.doi.org/10.1190/geo2014-0335.1>.
- Pimienta, L., Fortin, J., Guéguen, Y., 2015b. Experimental study of young's modulus dispersion and attenuation in fully saturated sandstones. *Geophysics* 80, L57–L72. <http://dx.doi.org/10.1190/geo2014-0532.1>.
- Pritz, T., 1994. Dynamic young's modulus and loss factor of plastic foams for impact sound isolation. *J. Sound Vib.* 178, 315–322. <http://dx.doi.org/10.1006/jsvi.1994.1488>.
- Pritz, T., 1998. Frequency dependences of complex moduli and complex Poisson's ratio of real solid materials. *J. Sound Vib.* 214, 83–104. <http://dx.doi.org/10.1006/jsvi.1998.1534>.
- Pujol, J.M., Luschen, E., Hu, Y., 1998. Seismic wave attenuation in metamorphic rocks from VSP data recorded in Germany's continental super-deep borehole. *Geophysics* 63 (354), <http://dx.doi.org/10.1190/1.1444335>.
- Quintal, B., Rubino, J.G., Caspari, E., Holliger, K., 2016. A simple hydromechanical approach for simulating squirt-type flow. *Geophysics* 81, D335–D344. <http://dx.doi.org/10.1190/geo2015-0383.1>.
- Quintal, B., Steeb, H., Frehner, M., Schmalholz, S.M., 2011. Quasi-static finite element modeling of seismic attenuation and dispersion due to wave-induced fluid flow in poroelastic media. *J. Geophys. Res.: Solid Earth* 116. <http://dx.doi.org/10.1029/2010JB007475>.
- Ramsay, J.G., Huber, M.I., 1987. *The Techniques of Modern Structural Geology: Folds and Fractures, Vol. 2*. Academic Press.
- Reksowardojo, A.P., Senatore, G., Srivastava, A., Carroll, C., Smith, I.F., 2022. Design and testing of a low-energy and -carbon prototype structure that adapts to loading through shape morphing. *Int. J. Solids Struct.* 252, 111629. <http://dx.doi.org/10.1016/j.ijsolstr.2022.111629>.
- Rubino, J.G., Guarracino, L., Müller, T.M., Holliger, K., 2013. Do seismic waves sense fracture connectivity?. *Geophys. Res. Lett.* 40, 692–696. <http://dx.doi.org/10.1002/grl.50127>.
- Schmalholz, S., Podladchikov, Y., 1999. Buckling versus folding: importance of viscoelasticity. *Geophys. Res. Lett.* 26, 2641–2644. <http://dx.doi.org/10.1029/1999GL900412>.
- Schüler, T., Manke, R., Jänicke, R., Radenberg, M., Steeb, H., 2013. Multi-scale modelling of elastic/viscoelastic compounds. *ZAMM - J. Appl. Math. Mech.* / *Z. Angew. Math. Mech.* 93, 126–137. <http://dx.doi.org/10.1002/zamm.201200055>.
- Shafiro, B., Kachanov, M., 1997. Materials with fluid-filled pores of various shapes: Effective elastic properties and fluid pressure polarization. *Int. J. Solids Struct.* 34, 3517–3540. [http://dx.doi.org/10.1016/S0020-7683\(96\)00185-0](http://dx.doi.org/10.1016/S0020-7683(96)00185-0).
- Shapiro, S.A., 2013. The Pressure Dependence of Permeability as a Function of Stiff and Compliant Porosities. ASCE, pp. 2500–2509. <http://dx.doi.org/10.1061/9780784412992.291>, (Chapter 291).
- Steeb, H., 2010. Ultrasound propagation in cancellous bone. *Arch. Appl. Mech.* 80, 489–502.
- Subramaniyan, S., Quintal, B., Madonna, C., Saenger, E.H., 2015. Laboratory-based seismic attenuation in fontainebleau sandstone: Evidence of squirt flow. *J. Geophys. Res.: Solid Earth* 120, 7526–7535. <http://dx.doi.org/10.1002/2015JB012290>.
- Tisato, N., Quintal, B., 2013. Measurements of seismic attenuation and transient fluid pressure in partially saturated Berea sandstone: Evidence of fluid flow on the mesoscopic scale. *Geophys. J. Int.* 195, 342–351. <http://dx.doi.org/10.1093/gji/ggt259>.
- Ungureanu, B., Achaoui, Y., Enoch, S., Brûlé, S., 2015. Auxetic-like metamaterials as novel earthquake protections. *EPJ Appl. Metamat.* 2, 1–8.
- Ursin, B., Toverud, T., 2002. Comparison of seismic dispersion and attenuation models. *Stud. Geophys. Geod.* 46, 293–320. <http://dx.doi.org/10.1023/A:1019810305074>.
- Vinci, C., Renner, J., Steeb, H., 2014. On attenuation of seismic waves associated with flow in fractures. *Geophys. Res. Lett.* 41, 7515–7523. <http://dx.doi.org/10.1002/2014GL061634>.
- Wang, H.F., 2000. *Theory of Linear Poroelasticity with Applications to Geomechanics and Hydrogeology*. In: *Princeton Series in Geophysics*, Princeton University Press.
- White, J.E., Mihailova, N., Lyakhovitsky, F., 1975. Low-frequency seismic waves in fluid-saturated layered rocks. *J. Acoust. Soc. Am.* 57, S30. <http://dx.doi.org/10.1121/1.1995164>.
- Würsig, B., Jr., C.G., Jefferson, T., 2000. Development of an air bubble curtain to reduce underwater noise of percussive piling. *Mar. Environ. Res.* 49, 79–93. [http://dx.doi.org/10.1016/S0141-1136\(99\)00050-1](http://dx.doi.org/10.1016/S0141-1136(99)00050-1).